processes

MDPI

Article

Effective Malachite Green Degradation over the Noble Metal-Doped and MOF-Coupled $CsSnBr_3$ Nanocomposite Catalyst

Bohan Ai [1,2], Mingsheng Luo [1,2,*] and Iltaf Khan [1,3]

[1] College of New Materials and Chemical Engineering, Beijing Institute of Petrochemical Technology, 19 Qing-Yuan North Road, Beijing 102617, China
[2] Beijing Key Laboratory of Fuels Cleaning and Advanced Catalytic Emission Reduction Technology, Beijing Institute of Petrochemical Technology, 19 Qing-Yuan North Road, Beijing 102617, China
[3] School of Environmental & Chemical Engineering, Jiangsu University of Science and Technology, 666 Changhui Road, Zhenjiang 212100, China
* Correspondence: luoms9297@163.com

Abstract: Environmental protection laws require effective and green solutions to tackle water and air pollution issues. For this purpose, perovskite photocatalytic materials have proven to be a promising solution. In this study, $CsSnBr_3$ perovskite, coupled with ZIF-67 and decorated with noble metal Au, was shown to effectively enhance the charge separation and increase the light-absorbing capacity, and thus make the photocatalytic reaction more efficient by surface plasmon resonance. Characterization results from XRD, FTIR, and UV-visible diffuse reflectance spectroscopy indicated that a mixture of cubic and tetragonal crystalline phases was found in the prepared catalyst material. XPS also revealed that in the presence of two oxidation states for tin (Sn), the Au 4f XPS peaks of Au NPs coincided with those retained in colloidal Au particles. Using malachite green as a model compound, organic pollutant photocatalytic degradation tests proved that $CsSnBr_3$ generated good photocatalytic activity for aromatic pollutant degradation. In this research, the synthesized 4Au-7ZIF-$CsSnBr_3$ catalyst yielded an MG degradation rate twice as high as the unpromoted $CsPbBr_3$.

Keywords: photocatalytic degradation; malachite green pollution; ZIF-67; $CsSnBr_3$ catalyst; Au promoter; nanocomposite catalyst

Citation: Ai, B.; Luo, M.; Khan, I. Effective Malachite Green Degradation over the Noble Metal-Doped and MOF-Coupled $CsSnBr_3$ Nanocomposite Catalyst. *Processes* **2023**, *11*, 1398. https://doi.org/10.3390/pr11051398

Academic Editors: Kang Hyun Park, Sungkyun Park and Ji Chan Park

Received: 3 April 2023
Revised: 25 April 2023
Accepted: 2 May 2023
Published: 5 May 2023

1. Introduction

Aromatic pollutants from various consumer products and coal combustion are currently a serious environmental issue [1]. The release of organic pollutants such as malachite green (MG) into water bodies causes severe harm to human health and the ecosystem. Solar energy is a clean and sustainable source of energy, and the development and deployment of photovoltaic solar cells is an effective solution to the energy and environmental problems [2]. The photocatalytic technique involves the use of solar energy; the photocatalyst is excited via absorption of light to produce electron–hole pairs to initiate redox reactions. More specifically, materials such as ABX_3 (A = Rb, Cs; B = Ge, Sn, Pb; X = Cl, Br, I) are halide perovskites (PVKs), which have outstanding intrinsic properties, such as a high light absorption coefficient, long service life, and simple preparation process [3]. PVKs have also garnered growing interest in the development of new solar cell research [4–6].

All-inorganic perovskite $CsPbX_3$ (X = I, Br, Cl) was once believed to be a promising substitute for organic–inorganic perovskites [7]. However, the lead component is toxic to human and damaging to the environment. Replacing lead with tin at the B-site to prepare a lead-free, environmentally friendly perovskite catalyst can obviate the pollution issue and, thus, expand the application of the new catalyst [8,9]. As a result, there has been a great deal of interest in replacing lead with nontoxic metals such as tin, bismuth, or

germanium. Remarkably, among various PVKs, $CsSnBr_3$ is believed to be a promising material, providing an innovative platform for pollution control applications [10].

Nevertheless, the organic pollutant degradation in wastewater treatment over the halide perovskite catalyst still needs more thorough research to improve the reaction efficacy for commercial application. Coupling halide PVKs with other materials to facilitate the charge separation may be an effective strategy to enhance the catalytic performance [11]. The composite of different materials of conventional photocatalysts can also degrade the pollutants in the dye form to a good degree [12,13]. The stability of halide PVK can be greatly improved by embedding it into protective materials such as polymers and amorphous metal oxides. In addition, porous materials, including mesoporous silica, metal–organic framework materials (MOFs), and zeolites, have been reported as useful for confining the PVK nanocrystals inside of the pores, with precise microstructure control and active metal dispersion [14].

To address the issue of low surface area and low charge separation, ZIF-67 was selected as a template material to enhance the catalytic performance of the PVK type of catalyst. As an MOF material, ZIF-67 shows good visible-light photocatalytic activity due to its narrow band gap of about 1.98 eV, offering a good visible-light response as well as the desired surface area, porous structure, adjustable organic ligands, and polymetallic sites. Thus, the incorporation of ZIF-67 in the PVK catalyst leads to a high surface area, while the MOF material can also act as an electron acceptor to enhance photo-generated electrons via photoelectron modulation strategies [15].

Promotion by noble metal nanoparticles such as Au and Ag can play a critical role in improving the light absorption and charge separation due to the surface plasmon resonance (SPR) [16]. Promotion by both the MOF materials and the metallic metals can, thus, effectively promote the photocatalytic activities of $CsSnBr_3$ for MG and other organic pollutant degradation. Panahi P. and Rasoulifard M. found that Ag-doped $LaCoO_3$ produced a remarkable photocatalytic malachite green removal rate of (80%) [17]. Similarly, Varun and Augustus confirmed that the optimized 20%TiO_2-NiO sample generated an 88% degradation rate for malachite green [18]. This makes the noble metal and MOF-promoted $CsSnBr_3$ nanocomposite catalyst a promising candidate for pollutant treatment.

2. Experimental

The chemicals and reagents were purchased from Macklin Biochemical Technology Co., Ltd. (Shanghai, China) and Aladdin Holdings Group Co., Ltd. (Beijing, China). These reagents and their chemical formulae or acronyms are listed in Table 1. All chemicals were used as received in this study, with no further pretreatment.

Table 1. Chemicals and suppliers.

Reagent Name	Chemical Formula or Acronym	Purity	Manufacturer
Tin(II) bromide	$SnBr_2$	99.0%	Macklin
1-Octadecene	ODE	≥95.0%	Macklin
Oleic acid	OA	AR	Macklin
Octadecenylamine	OLAM	80–90%	Macklin
Cesium carbonate	Cs_2CO_3	99.0%	Macklin
Trioctylphosphine oxide	TOPO	98.0%	Macklin
Diethylenetriamine	DETA	99.0%	Macklin
Lead bromide	$PbBr_2$	99.0%	Macklin
Cesium bromide	CsBr	99.5%	Macklin
N,N-dimethylformamide	DMF	99.5%	Macklin
Cobalt nitrate hexahydrate	$Co(NO_3)_2{\cdot}6H_2O$	99.0%	Macklin
Malachite green	MG	AR	Macklin
2-methylimidazole	$C_4H_6N_2$	98.0%	Aladdin
Chloroauric acid	$HAuCl_4{\cdot}4H_2O$	99.0%	Aladdin

2.1. Catalyst Synthesis

2.1.1. Synthesis of $CsSnBr_3$

Firstly, 0.7 g of $SnBr_2$, 60 mL of ODE, 6 mL of OA, and 6 mL of OLAM was added to a 100 mL 4-neck flask. The flask was placed into a 120 °C vacuum dryer for 1 h, and the resulting solution was labeled as sample A. Then, 2 g of Cs_2CO_3 was dissolved in 50 mL of ODE and 5 mL of OA heated at 120 °C, with vigorous agitation for 1 h. This latter sample was labeled as reagent B. After that, 1 mL hydrochloric acid, 0.2 g TOPO and 10 mL DETA were mixed with 10 mL A and 5 mL B, then heated at 80 °C for 1 h with vigorous stirring and continuous nitrogen purging. The aforementioned reagent was placed into a 50 mL autoclave, and DETA was added for a total volume of 40 mL inside the vessel. The autoclave was sealed and settled at 180 °C for 6 h before the solution was quickly cooled down to ambient temperature in an ice bath. The sample were quickly transferred to a centrifuge bottle inside of an air-tight glovebox. After the solution was then centrifuged, filtered, and washed by excessive acetone, distilled water, and toluene stepwise, the sample was placed into a 80 °C vacuum dryer for 12 h. The obtained dry sample was then dispersed in toluene or acetone for future use, as suggested in the literature [19].

2.1.2. Synthesis of $CsPbBr_3$

For the next step, 0.367 g $PbBr_2$ and 0.212 g CsBr were mixed in a 100 mL round-bottom flask along with 25 mL DMF, under vigorous stirring, for 30 min at room temperature until they were completely dissolved. Then, 2.5 mL of OA and 1.25 mL of OLAM were added to the flask, and the mixture was stirred continuously for 10 min. The resulting reagent was then carefully added dropwise into 50 mL toluene and centrifuged for 10 min at 10,000 r/min. The supernatant was removed before 50 mL toluene was added, then centrifuged one more time. The precipitate was vacuum-dried at 60 °C for 6 h, and the obtained $CsPbBr_3$ powder was ground using an agate mortar [20].

2.1.3. Synthesis of ZIF-67

Next, 0.873 g of $Co(NO_3)_2 \cdot 6H_2O$ was dissolved in 30 mL of methanol to prepare the solution labeled as sample A. Similarly, 1.97 g of 2-methylimidazole was dissolved in 25 mL methanol to prepare the solution labeled as B. Solution B was quickly added to solution A, and the mixture was continuously stirred at room temperature for 24 h. The obtained bright purple precipitate was filtrated and then washed with 20 mL methanol. After being dried at 60 °C for 12 h, the powdered ZIF-67 material was thus prepared [21].

2.1.4. Synthesis of ZIF67-$CsSnBr_3$ Nanocomposite

Using 1 g of $CsSnBr_3$, a series of XZIF-67 catalyst samples were prepared with different mass ratios of ZIF-67 to $CsSnBr_3$, where X represents the mass percentage ratio. Mixtures of different amounts of ZIF-67 with 1 g of $CsSnBr_3$ were added to a solution containing 5 mL of methanol and 5 mL of deionized water. The solution was vigorously stirred for 1 h, followed by ultrasonic agitation for another hour. The resulting sample was then dried in a 100 °C oven for 10 h. The synthesized samples were denoted with XZIF-$CsSnBr_3$, where X represents the different mass percentages (1, 3, 5, 7, or 9%) of ZIF-67 relative to the mass of $CsSnBr_3$, as suggested in the literature [22].

2.1.5. Au-Promoted ZIF-$CsSnBr_3$

To prepare the 1, 4, and 7 wt% Au-promoted XZIF-$CsSnBr_3$ catalysts, 1 g XZIF-$CsSnBr_3$ was added to 3 different volumes of 0.1 M $HAuCl_4$ solutions as the Au precursor. A mixture of 5 mL methanol and 5 mL deionized water was added to the mixture of $HAuCl_4$ and XZIF-$CsSnBr_3$. The resulting solution was then transferred to a 100 mL round-bottom flask. With vigorous stirring at 300 r/min and continuous nitrogen purging through the liquid mixture for 30 min to remove the dissolved oxygen and to avoid the reduction of Au nanoparticles, the mixture was centrifuged and dried in a 50 °C oven for 12 h. To keep it from decomposing by visible light, the mixture was fully covered with aluminum

foil during the entire process. The thus-synthesized samples were designated as YAu-XZIF-$CsSnBr_3$, where Y stands for the mass percentage of Au relative to the XZIF-$CsSnBr_3$ material used. Three different volumes of the solution (V) needed for each of the three Au promoted catalysts, as well as the wt% amount of Au in each of the prepared catalysts, can be calculated by the following equation, as suggested in the literature.

$$Y = \frac{C * M * V}{1000 * Y * W}$$

where W is the weight of XZIF-$CsSnBr_3$ (1 g for all 3 samples), C is the concentration of the $HAuCl_4$·solution (0.1 M for all 3 samples), Y is the mass ratio of Au to $CsSnBr_3$ (wt%), and M is the molecular weight of Au (197 g/mol).

2.2. Characterization of Materials

An X-ray diffractometer (XRD, Rigaku D/MAX-RA Shimadzu, Kyoto, Japan) was used to determine the crystal structure of the prepared samples under the conditions of 20 kV and 10 mA current. An X-ray photoelectron spectroscopy (XPS) (Thermo ESCALAB 250XI Kratos-Axis Ultra DLD Shimadzu, Kyoto, Japan.) apparatus was used to assess the surface chemical properties of the sample using an Al kα ray (hν = 1486.6 eV) radiation source, with the analysis chamber operated under 4×10^{-9} mbar vacuum. The binding energy (BE) and kinetic energy (KE) scales were adjusted by setting the C1s transition at 284.6 eV, and the BE and KE values were then determined with the peak-fit software of the spectrometer.

The FTIR spectra of the sample were measured via Bruker Tensor II (Equinox 55 Germanany.in the 400–4000 cm^{-1} wavenumber range. KBr powders were used as diluents for sample preparation and for reference. BELSORP-max was used to obtain the BET surface area and pore size distribution data.

2.3. Photocatalytic Degradation Activity Test

As shown in Figure 1, a sample of 10 mg of malachite green was dissolved in 1.00 L of distilled water to prepare a 0.01 M malachite green solution. For each experiment, 0.200 g of the catalyst sample was mixed with 100 mL of the solution under continuous stirring in a dark box for 30 min to achieve absorption equilibrium. To evaluate the photocatalytic activities of the samples, the reactor containing MG, H_2O, and catalysts was irradiated with visible light using a 300 W xenon lamp purchased from Beijing, China and a 420 nm cutoff filter. At fixed intervals of 30 min, 5 mL of the solution was collected using a syringe and filtered. The solution was transferred into a 10 mL sample vial to obtain UV-visible spectra data from the HITACHI U-3900 spectrophotometer (UV-2550 Shimadzu Corporation Shimadzu, Kyoto, Japan). The stability of the photocatalysts for photocatalytic MG degradation was determined by the same procedure [23].

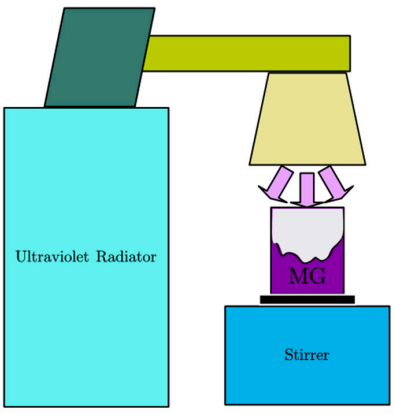

Figure 1. Photocatalytic reaction evaluation system.

3. Results and Discussion

3.1. The Advantages of CsSnBr3 over CsPbBr3

$CsSnBr_3$ was synthesized by the hydrothermal method, and $CsPbBr_3$ through room-temperature, supersaturated recrystallization. However, from the environmental point of view, Pb is a globally considered as a harmful element. This has led to great interest in replacing it with non- or low-toxic metals, and among the potential substitutes, tin (Sn) is a possible candidate [24–26]. Figure 2A shows XRD data for the two catalysts observed in this study, i.e., $CsSnBr_3$ and $CsPbBr_3$. Peaks of the cubic phase were found at 21°, 31°, 34°, and 46°, which were assigned to the reflections of planes (100), (110), (111), and (200), respectively. There were other peaks showing the tetragonal perovskite crystalline phase, which appeared at about 16°, 26°, and 39°. Notably, the transition between the two crystalline phases for the perovskite occurs at about 19 °C. The test was conducted at room temperature and, thus, yielded these two crystal phases [27]. Furthermore, a minor variation at the edge of the DRS band indicated that $CsSnBr_3$ was situated in the visible region, suggesting that $CsSnBr_3$ exhibits better charge separation than $CsPbBr_3$.

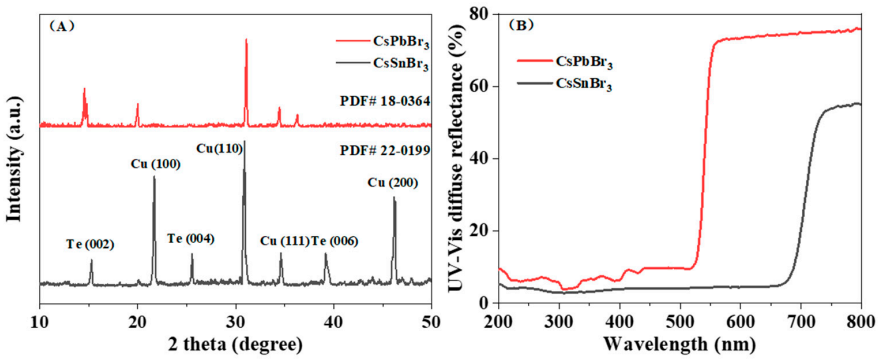

Figure 2. XRD patterns (**A**) and UV-visible DRS spectra of $CsSnBr_3$ and $CsPbBr_3$ (**B**).

To further verify the superior catalytic performance of $CsSnBr_3$ to the $CsPbBr_3$ catalyst, the samples were evaluated for their catalytic activity in MG degradation. It can be seen in Figure 3 that the activity of $CsSnBr_3$ was nearly twice as high than that of $CsPbBr_3$. These results clearly prove that the $CsSnBr_3$ catalyst is more active and more stable than the $CsPbBr_3$ sample.

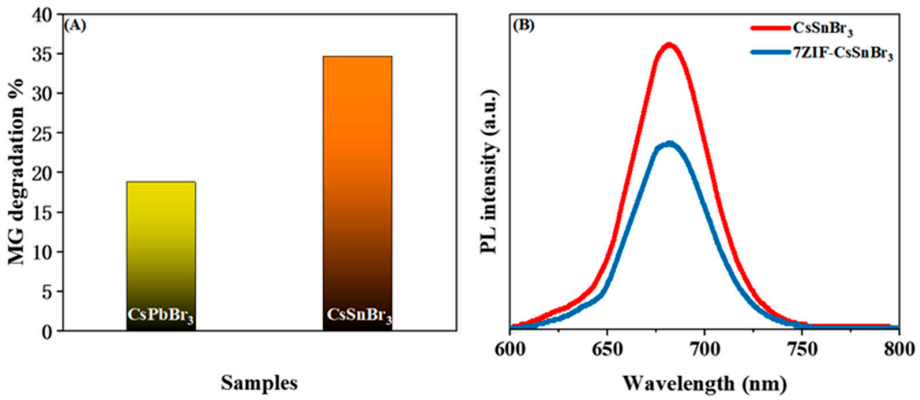

Figure 3. Visible-light activities for malachite green degradation rate of $CsSnBr_3$ and $CsPbBr_3$ (**A**), PL spectra representing charge separation (**B**).

3.2. Efficacy of Metal–Organic Framework (ZIF-67)

ZIF-67, known as zeolitic imidazolate framework-67, is a type of metal–organic framework (MOF) material that is composed of metal ions coordinated with organic ligands to form a porous structure. Specifically, ZIF-67 is composed of cobalt ions coordinated with

imidazolate ligands to form a three-dimensional network with a high surface area and pore volume. The unique properties of ZIF-67, such as its high stability, tunable pore size, and high surface area, make it useful in various applications, such as gas separation, catalysis, and sensing. For example, ZIF-67 has been used as a selective adsorbent for CO_2, as a catalyst for organic reactions, and as a sensor for detecting trace amounts of volatile organic compounds [28]. A high surface area of ZIF-67 provides a large number of active sites for catalytic reactions with high photocatalytic efficiency. The porous structure of ZIF-67 facilitates the diffusion of reactants and products, resulting in enhanced photocatalytic reactions. Some properties of ZIF-67, such as the band gap, can be tuned by varying the composition and structure of the material, making it possible to tailor its photocatalytic properties for some applications [29–31].

Studies have shown that MOFs should be applied in the field of photocatalysis to be combined with photosensitive molecules or photocatalytic active centers to generate excellent photocatalytic properties. By introducing specific ligands or metal-centric ions into the structures of MOFs, the light absorption properties can be improved. In this context, MOFs can be used in photocatalytic water decomposition, degradation of organic pollutants, CO_2 reduction, and other reactions that usually require highly controllable catalysts. ZIF-67, consisting of Co^{2+} and ligand of 2-methylimidazole, offers a wide range of applications in photocatalysis for its porous and highly adjustable structure [32,33]. The porous structure of ZIF-67 can provide more light-absorbing surfaces, thus increasing the interaction between reactant molecules and photons. In addition, the special arrangement of the metal center ions and ligand molecules can produce a resonance effect, further improving the light absorption capacity of ZIF-67. The structure can effectively promote charge separation and transfer, thus increasing the efficacy of the reaction [34]. Under irradiation, the metal center ions and ligand molecules can generate charge pairs that can be rapidly transported and separated through electron transport pathways within the porous structure. This structure can be enhanced by the introduction of photocatalytic active components, such as metal core ions, ligand molecules, or other catalytic components. These catalytic sites can enhance the adsorption of reactant molecules, thus reducing the energy barrier of the reaction and increasing the reaction rate. Its photocatalytic activity and stability can be improved by surface modification or by compositing with other materials.

In this study, the highly efficient and specific surface area metal–organic framework (ZIF-67) was thus prepared to further improve the properties of the existing catalysts. Figure 3B shows that coupling of ZIF-67 with the catalyst can not only enhance the charge separation, but also improve the photocatalytic activity. For this purpose, various types of physicochemical characterizations were carried out by the XRD and TEM to obtain information on the crystallinity, functional groups, absorbance points, and surface area of the catalyst [35]. As shown in the FITR spectra, the peak at 2922.83 cm^{-1} indicates the stretching vibration of aliphatic C-H of methyl imidazole, while the peaks at 1633.787 and 1416.98 cm^{-1} represent the C=N and C=C groups of imidazole, respectively. In addition, the peak at 3439.39 cm^{-1} is related to the hydroxyl groups (O-H) [36]. The N_2-adsorption/desorption isotherm in Figure 4 reveals a reversible type I isotherm, suggesting a characteristic microporous structure. A plateau appears after certain uptake of gas at a lower pressure, indicating that a multilayer adsorption has been formed and no more pores are left for additional gas uptake. The BET area of the as-synthesized ZIF-67 sample is 1600 m^2/g and the mean pore diameter is 1.78 nm, as obtained from the BET test.

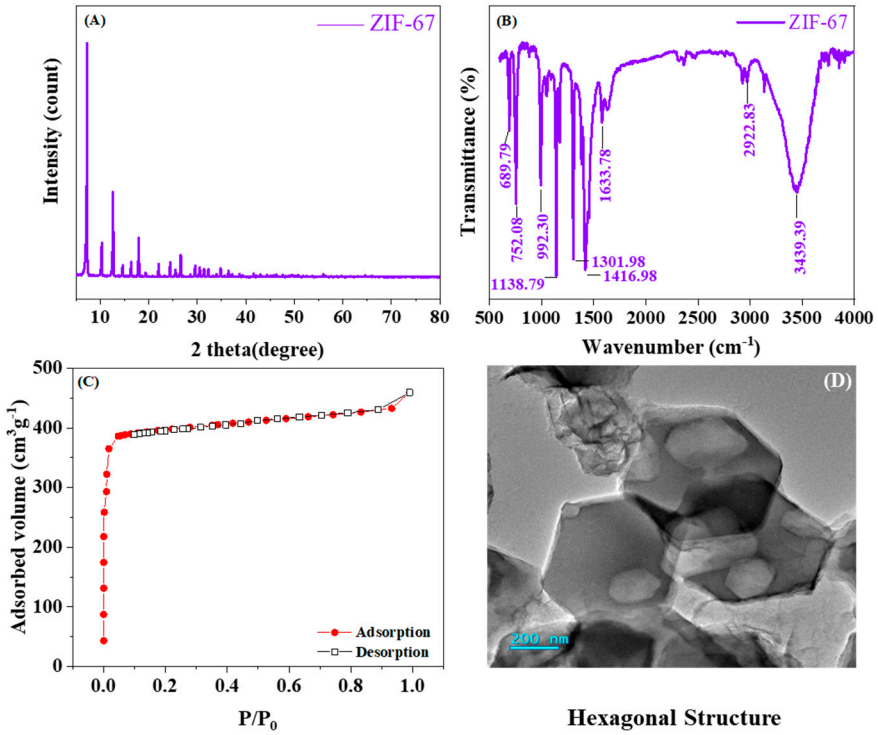

Figure 4. XRD pattern (**A**), FTIR spectra (**B**), N_2 adsorption–desorption isotherm (**C**), and TEM images (**D**) of ZIF-67.

3.3. Compositing ZIF-67 with $CsSnBr_3$

Although unsatisfied porosity and low light absorption were improved, the $CsSnBr_3$ catalyst still encounters problems, such as its small surface area and low charge separation. The use of ZIF-67, a metal–organic framework, offers an advantageous solution to these issues due to its superior properties, such as surface area, regular porous structure, adjustable organic ligands, and proper band gap position, as well as its multiple metallic active sites [37]. Thus, the combination of ZIF-67 with existing catalysts can improve the specific surface area, while the MOF material can, in the meantime, serve as an electron acceptor to facilitate photo-generated electrons via photoelectron modulation. ZIF-67 was thus used to couple with $CsSnBr_3$ in this study. The color of the as-prepared powders changed from vivid yellow to grayish green, and then to green-yellow, with the increasing ZIF-67 content.

The unique properties of MOFs, such as their high porosity, large surface area, and adjustable pore size, make them ideal candidates for the photocatalytic degradation of pollutants. The photoexcited electrons and holes can react with the adsorbed pollutant molecules, leading to the formation of reactive oxygen species (ROS) such as hydroxyl radicals (•OH) and superoxide radicals ($\bullet O^{2-}$). These ROS can effectively oxidize the pollutant molecules, breaking them down into smaller, harmless compounds, such as carbon dioxide and water. The MOF material can act as a catalyst to facilitate the reaction between the photoexcited electrons and holes and the adsorbed pollutant molecules. The catalytic activity of the MOF material can be enhanced by modifying its surface properties, in ways such as introducing functional groups or metal dopants.

XRD data indicate that a distinct peak can be observed after combining different amount of ZIF, as shown in Figure 5A. The UV-DRS spectra reveal that the optical absorption edges remained unchanged after adding ZIF to Au-$CsSnBr_3$, as shown in Figure 5B, which is in good agreement with some other studies.

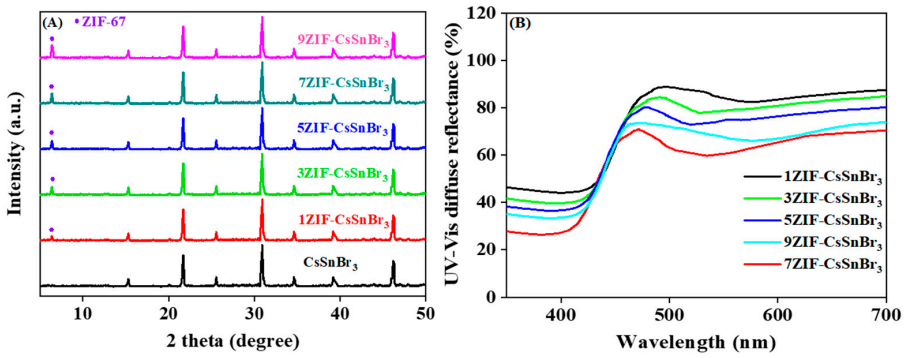

Figure 5. XRD patterns (**A**); UV-visible DRS spectra (**B**) of the XZIF- $CsSnBr_3$ nanocomposites.

The as-prepared samples were evaluated for MG degradation, and the results from Figure 6 show that XZIF-$CsSnBr_3$ (x = 1, 3, 5, 7, and 9) yielded the highest photocatalytic activities among all catalysts prepared in the previous steps, at 180 min of optimized reaction time. These results clearly confirm the significant enhancement of activity by the new synthesized catalyst, pointing towards MG degradation. After five cycles of reaction runs, it can also be confirmed that the as-prepared samples were highly stable for the MG degradation reaction.

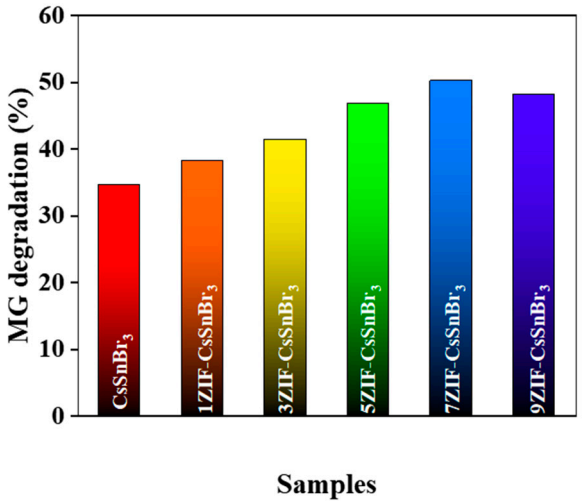

Figure 6. Visible-light activity for the malachite green degradation rate of XZIF-$CsSnBr_3$.

3.4. The Effects of Incorporating ZIF-$CsSnBr_3$ into Au SPR Nanoparticles

In this study, despite the surface area of the prepared $CsSnBr_3$, it still required some other improvement, such as limited visible light absorption, which influenced its photocatalytic activity. To solve these issues, the prepared $CsSnBr_3$ was promoted with Au. Different amounts of $HAuCl_4$ solution, namely, 1, 4, and 7 mL, were used to prepare 3 different Au mass contents of 1.97, 7.88, and 13.79% of the catalyst in order to investigate the promotional effect of gold.

Studies have shown that the photocatalytic effect of noble metals, such as Au, combined with MOFs can be improved. Gold nanoparticles can be used as plasmonic photocatalysts to enhance the photocatalytic activity of semiconductor materials [38]. When exposed to light, gold nanoparticles can generate localized surface plasmons (LSPs), which can interact with the semiconductor material and promote the absorption of light and the generation of charge carriers. This leads to enhanced photocatalytic activity, particularly in the visible light region, where many semiconductor materials have low absorption [39].

Surface plasmon resonance (SPR) allows light to interact with a thin metal film or surface, and creates a collective oscillation of free electrons called a surface plasmon [40].

The SPR properties of gold nanoparticles can be used for the sensing and detection of target molecules or analytes in photocatalytic systems [41–43]. Gold nanoparticles can be functionalized with specific ligands or receptors to selectively bind to the target molecules, and the binding effect can be detected by changes in the SPR signal. The photocatalytic performance of the catalyst is improved by the SPR of these nanoparticles or thin film materials [44]. These materials have large surface areas and superior photocatalytic response characteristics [45]. When the catalyst interacts with visible light, the SPR phenomenon can be observed, which is induced by the interaction of metal nanoparticles with light [46,47]. This can, thus, increase the light-absorbing capacity and improve the photocatalytic activity. The resonant vibration creates a strong electric field on the surface of the metal nanoparticles, and the photons interact with electrons in the catalyst [48]. The SPR-induced interaction between the light and the metal thin film is highly sensitive to changes in the refractive index of the material in contact with the metal surface [49]. SPR occurs in photocatalysis based on the creation of LSPs when light is absorbed by a metal nanoparticle or a metal film deposited on the surface of the semiconductor material [50,51]. LSPs create a strong electromagnetic field near the metal's surface, which can then interact with the semiconductor material and enhance the absorption of light and the generation of charge carriers, thus improving the photocatalytic activity.

The addition of Au nanospheres promotes the rate of exciton generation and the probability of exciton dissociation, charger separation, and transfer. Organic pollutants can be effectively degraded through the catalytic function provided by the noble metal Au. The crystallinity of the YAu-XZIF-$CsSnBr_3$ nanocomposite was obtained with XRD. The results are shown in Figure 7A, suggesting the successful synthesis of the catalyst sample containing ZIF-67 and the Au site. The UV-Vis diffused reflection spectra of the samples are shown in Figure 7B. Two sharp increases in the reflectance can be observed at about 500 and 580 nm. The increase in reflectance at about 580 nm can be assigned to the perovskite structure. Meanwhile, an intense absorption band is located at 580 nm, which can be assigned to the SPR of Au nanoparticles. It can be seen that increasing Au loading enhanced the light absorption of XZIF-$CsSnBr_3$; it has been suggested by other studies that the absorption intensity heightens along with increased Au doping amounts, within a certain range [52].

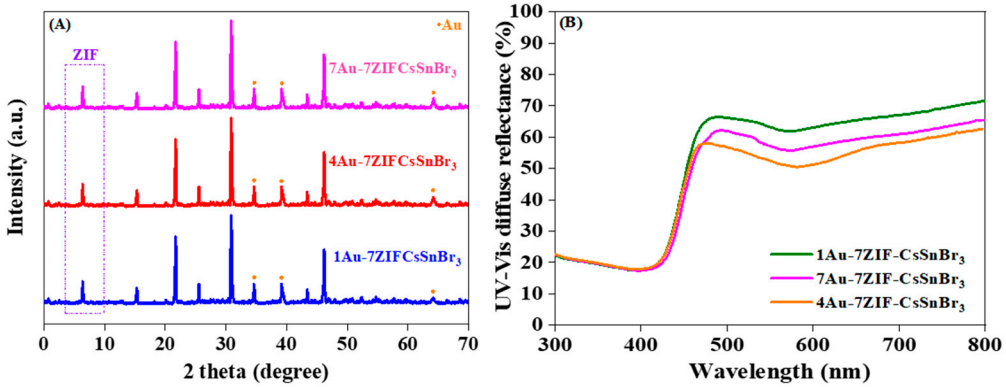

Figure 7. XRD patterns (**A**); UV-visible DRS spectra (**B**) of YAu-7ZIF-$CsSnBr_3$ nanocomposites.

To examine the morphology and structural characteristics of the prepared samples, TEM was employed to reveal a well-coupled sample using ZIF-67, as depicted in Figure 8A. ZIF-67 offers a superior porous structure, and, as shown in Figure 8B, the distinct dots and circles confirm the presence of Au. These morphological data can obviously confirm that Au was successfully coupled with ZIF-$CsSnBr_3$.

To further understand the obtained catalyst samples, XPS was employed to detect the composition of the chemical elements the and surface chemical state of the YAu-7ZIF-$CsSnBr_3$as-synthesized sample. The binding energy in the XPS analysis was corrected for specimen charging by referencing carbon 1 s to 284.8 eV. It was indicated that the Au 4f

peak at 87 eV was detected for the Au-doped composite sample compared with the AU-free catalyst. Figure 9 shows high-resolution XPS spectra of the five primary elements in the samples. As shown in the graph, the binding energies of Br 3d, Sn $3d_{3/2}$, Sn $3d_{5/2}$, Cs $3d_{5/2}$, Co $2p_{1/2}$, and Co $2p_{3/2}$ were 69, 487, 496, 724, 794, and 780 eV, respectively. The Br 3d peak, as clearly observed in Figure 9B, displays overlapping spin–orbit components that are separated by approximately 1 eV. Consequently, a broader peak was detected than that in other components, likely resulting from the presence of both components. In addition, the Cs 4d signal was identified in the same spectra data. The signal for Cs 3d is depicted in Figure 9A, where a peak located at around 724 eV was detected, representing the typical value for the contribution of Cs $3d_{5/2}$ to Cs^+ ions. Figure 9C shows the high-resolution XPS spectrum for Sn 3d. Both spin–orbit components were observed, with a binding energy separation of approximately 8.5 eV. The Sn $3d_{5/2}$ signal displayed a full width at half maximum (FWHM) of around 2 eV, and the signal was subsequently deconvoluted to analyze the different oxidation states of Sn present in the sample. The Sn $3d_{5/2}$ signal can be attributed by the binding energy (BE) of 487 eV assigned to Sn (II) and the BE of 495 eV assigned to Sn (IV). The presence of O was also observed in the sample obtained from the XPS data. Figure 9E shows Au 4f, with the characteristic peaks at 84 and 87 eV ascribed to Au $4f_{7/2}$ and Au $4f_{5/2}$, respectively, and the 3 eV splitting of the 4f doublet indicates the Au species presented in the metallic state [53]. Notably, Au components may be merely dispersed on the surface of the $CsSnBr_3$ crystal without being doped into the crystal lattice, as per the XPS and TEM results. The peaks in the survey spectrum were clearly assigned, and the presence of the Cs, Sn, Co, and Br in the ZIF-67 was clearly confirmed.

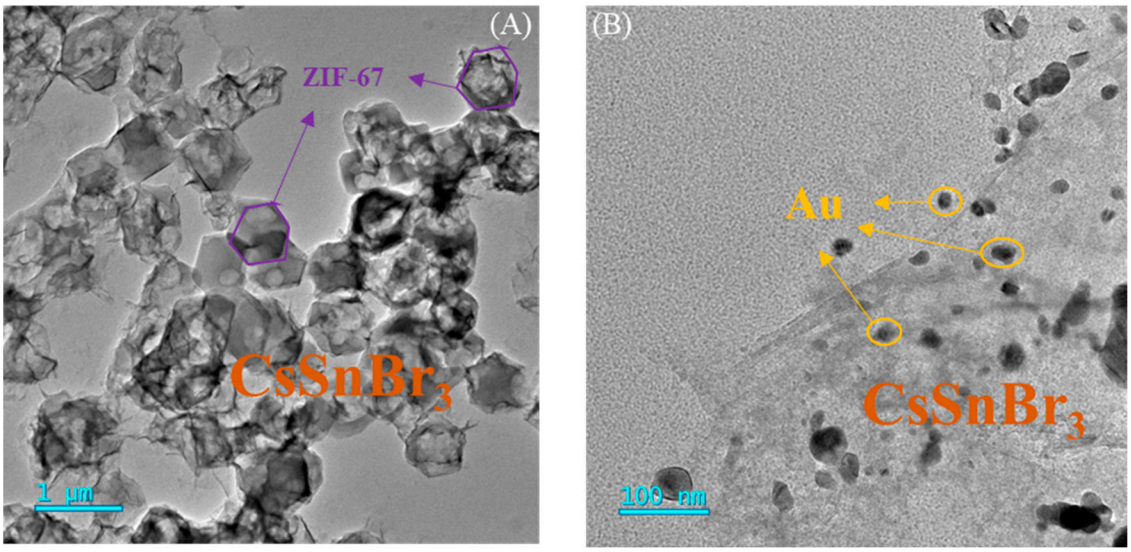

Figure 8. TEM images of ZIF-$CsSnBr_3$ (**A**) and Au-ZIF-$CsSnBr_3$ (**B**) nanocomposites.

Moreover, the photocatalytic activities of the catalyst sample were evaluated to assess the MG degradation reaction. After 5 cycles of the reaction runs, it was concluded that 150 min is the optimum reaction time to reach adsorption equilibrium, as shown in Figure 10A. The photocatalytic activity data of the synthesized samples for MG degradation under visible light irradiation are presented in Figure 10B. It is worth noting that the introduction of varying amounts of Au leads to a substantial increase in the photocatalytic activity of YZIF67-$CsSnBr_3$. As shown in the figure, the 4Au-7ZIF-$CsSnBr_3$ showed the optimum photocatalytic activity for MG degradation.

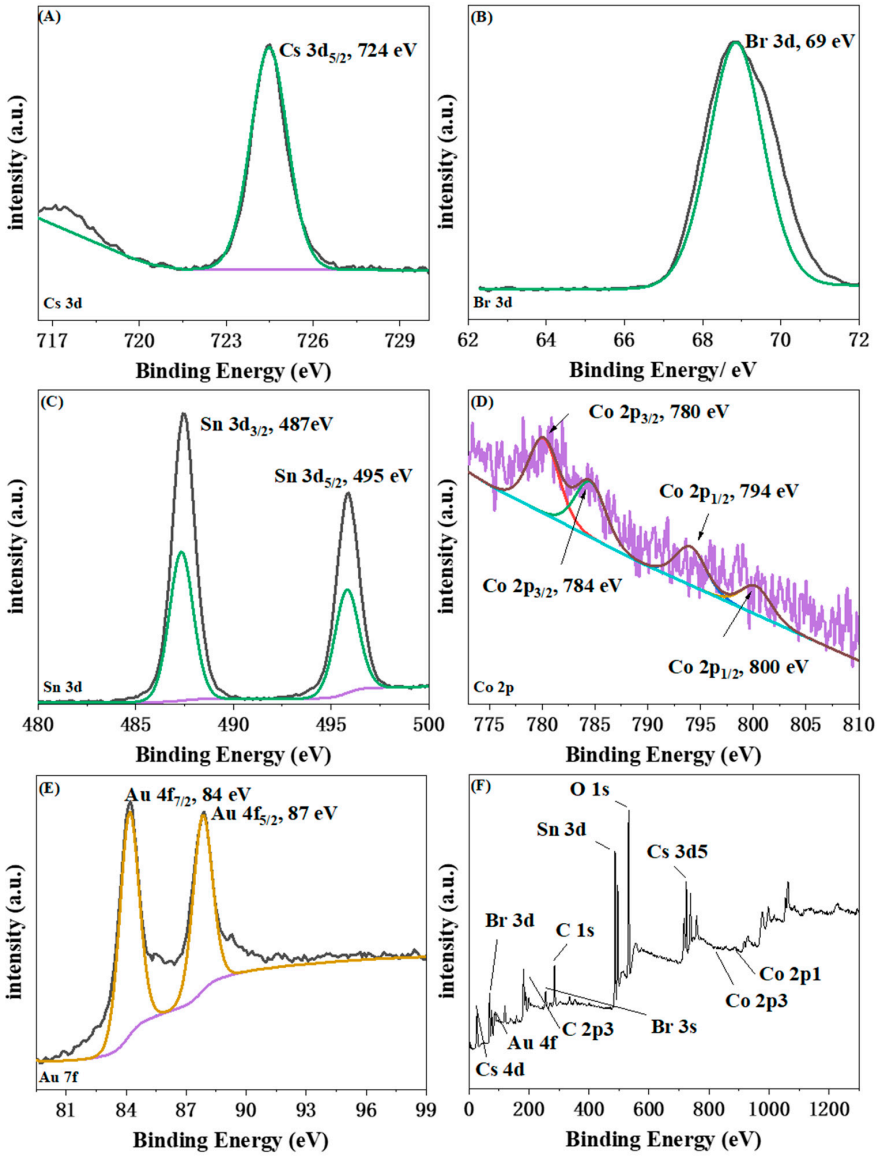

Figure 9. XPS spectra: (**A**) Cs 3d, (**B**) Br 3d, (**C**) Sn 3d, (**D**) Co 2p, (**E**) Au 7f, and (**F**) survey spectrum.

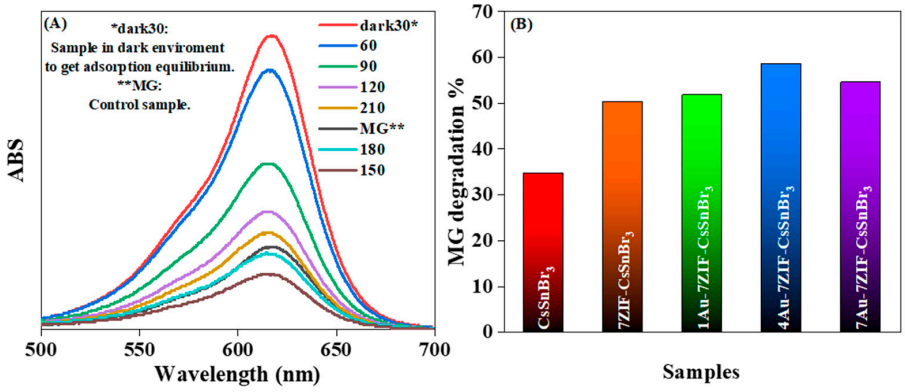

Figure 10. UV-Vis spectra of MG degradation (**A**), visible-light activity of malachite green degradation (**B**) of YAu-7ZIF-$CsSnBr_3$.

4. Conclusions

The synthesis of $CsSnBr_3$ was achieved through a simple solvothermal process in this research work. In addition, the noble metal Au was introduced into the system using photo-assisted deposition (PAD) [54]. The as-prepared nanocomposite was then coupled with the highly efficient and specific surface area metal–organic framework (ZIF-67) material used in the study. As per the results of this research, $CsSnBr_3$ shows remarkable opto-electronic properties, just as halide perovskite has remarkable opto-electronic properties such as optimal band structure, long charge carrier lifetimes, and high photoluminescence quantum yields [55]. In addition, the incorporation of Au in the $CsSnBr_3$ can effectively regulate its band gap through the SPR effect. Furthermore, combining it with MOF (ZIF-67) not only increases the surface area, but also considerably enhances the charge separation of $CsSnBr_3$ by modulating the mechanism of excited electron transfer [56].

These improvements facilitate the photocatalytic degradation reaction of MG. Moreover, by decorating the plasmonic noble metal Au, the band-gap position of ZIF-$CsSnBr_3$ was successfully shifted to a more visible region. The photocatalytic efficiency of the highly active 4Au-7ZIF-$CsSnBr_3$ nanocomposite was found to be twice as high for MG degradation when compared to an Au-free $CsSnBr_3$ catalyst. The method proposed in this study is based on perovskite, and aims to synthesize an improved catalyst by loading a metal promoter onto perovskite nanocrystals and by compositing MOF materials with the original $CsSnBr_3$ catalyst to improve the efficacy of photocatalytic pollutant degradation. This provides an important idea for the design of new perovskite nanocrystal types of catalysts. In future studies, more molecular calculation data and kinetic studies can be included in order to further elucidate the efficacy of the proposed catalyst. Parametric studies on the synthesis process may also be considered in future work for the purpose of improving the catalyst's design.

Author Contributions: B.A.: formal analysis; methodology; original draft preparation. M.L.: funding acquisition; review & validation; project administration; I.K.: methodology; visualization; software. All authors have read and agreed to the published version of the manuscript.

Funding: The authors are grateful for financial support from the Beijing Institute of Petrochemical Technology (15031862004-1).

Data Availability Statement: The data and materials that support the findings of this study are available from the corresponding author upon reasonable request.

Conflicts of Interest: The authors declare that they have no known competing financial interests or personal relationships that could have appeared to influence the work reported in this paper.

References

1. Liu, C.; Yu, L.Q.; Zhao, Y.T.; Lv, Y.K. Recent advances in metal-organic frameworks for adsorption of common aromatic pollutants. *Microchim. Acta* **2018**, *185*, 342. [CrossRef] [PubMed]
2. Park, N.G. Perovskite solar cells: An emerging photovoltaic technology. *Mater. Today* **2015**, *18*, 65–72. [CrossRef]
3. Kamat, P.V.; Bisquert, J.; Buriak, J. Lead-Free Perovskite Solar Cells. *ACS Energy Lett.* **2017**, *2*, 904–905. [CrossRef]
4. Liu, P.; Han, N.; Wang, W.; Ran, R.; Zhou, W.; Shao, Z.P. High-Quality Ruddlesden-Popper Perovskite Film Formation for High-Performance Perovskite Solar Cells. *Adv. Mater.* **2021**, *33*, e2002582. [CrossRef]
5. Kong, J.J.; Yang, T.; Rui, Z.B.; Ji, H.B. Perovskite-based photocatalysts for organic contaminants removal: Current status and future perspectives. *Catal. Today* **2019**, *327*, 47–63. [CrossRef]
6. Chandel, M.; Thakur, M.; Sharma, A.; Pathania, D.; Kumar, A.; Singh, L. Chlorophyll sensitized $(BiO)_2CO_3/CdWO_4$/rGO nanohybrid assembly for solar assisted photo-degradation of chlorzoxazone. *Chemosphere* **2022**, *305*, 135472. [CrossRef] [PubMed]
7. Protesescu, L.; Yakunin, S.; Bodnarchuk, M.I.; Krieg, F.; Caputo, R.; Hendon, C.H.; Yang, R.X.; Walsh, A.; Kovalenko, M.V. Nanocrystals of Cesium Lead Halide Perovskites ($CsPbX_3$, X = Cl, Br, and I): Novel Optoelectronic Materials Showing Bright Emission with Wide Color Gamut. *Nano Lett.* **2015**, *15*, 3692–3696. [CrossRef]
8. Bhaumik, S.; Ray, S.; Batabyal, S.K. Recent advances of lead-free metal halide perovskite single crystals and nanocrystals: Synthesis, crystal structure, optical properties, and their diverse applications. *Mater. Today Chem.* **2020**, *18*, 100363. [CrossRef]
9. Giustino, F.; Snaith, H.J. Toward Lead-Free Perovskite Solar Cells. *ACS Energy Lett.* **2016**, *1*, 1233–1240. [CrossRef]

10. Zhang, M.J.; Lin, Y.M.; Li, J.Y.; Wei, X.R.; Peng, Y.; Wang, Z.K.; Jiang, Z.Y. Interfacial Electronic and Photovoltaic Performance of a Novel Lead-Free Z-Scheme $CsSnBr_3/MoSe_2$ Perovskite Heterostructure: A Theoretical and Experimental Study. *Sol. RRL* **2022**, *7*, 2200784. [CrossRef]
11. Kumar, A.; Sharma, K.; Thakur, M.; Pathania, D.; Sharma, A. Fabrication of high visible light active $LaFeO_3$/Cl-g-C_3N_4/RGO heterojunction for solar assisted photo degradation of aceclofenac. *J. Environ. Chem. Eng.* **2022**, *10*, 108098. [CrossRef]
12. Sharma, A.; Pathania, D.; Kumar, A. Bio-Polymer Based Tragacanth Gum (TG) Loaded Fe_3O_4 Nanocomposite for the Sequestration of Tenacious Congo Red Dye from Waste Water. *J. Mater. Sci. Technol. Res.* **2020**, *7*, 92–100. [CrossRef]
13. Kumar, A.; Pathania, D.; Gupta, N.; Raj, P.; Sharma, A. Photo degradation of noxious pollutants from water system using *Cornulaca monacantha* stem supported $ZnFe_2O_4$ magnetic bio-nanocomposite. *Sustain. Chem. Pharm.* **2020**, *18*, 100290. [CrossRef]
14. Kong, Z.C.; Liao, J.F.; Dong, Y.J.; Xu, Y.F.; Chen, H.Y.; Kuang, D.B.; Su, C.Y. Core@Shell $CsPbBr_3$@Zeolitic Imidazolate Framework Nanocomposite for Efficient Photocatalytic CO_2 Reduction. *ACS Energy Lett.* **2018**, *3*, 2656–2662. [CrossRef]
15. Zhong, G.; Liu, D.; Zhang, J. The application of ZIF-67 and its derivatives: Adsorption, separation, electrochemistry and catalysts. *J. Mater. Chem. A* **2018**, *6*, 1887–1899. [CrossRef]
16. Humayun, M.; Ullah, H.; Shu, L.; Ao, X.; Tahir, A.A.; Wang, C.D.; Luo, W. Plasmon Assisted Highly Efficient Visible Light Catalytic CO_2 Reduction over the Noble Metal Decorated Sr-Incorporated g-C_3N_4. *Nanomicro Lett.* **2021**, *13*, 209. [CrossRef] [PubMed]
17. Panahi, P.N.; Babaei, S.; Rasoulifard, M.H. Synthesis and visible-light photocatalytic activity of nanoperovskites and exploration of silver decoration to enhance photocatalytic efficiency. *Desalination Water Treat.* **2020**, *194*, 194–202. [CrossRef]
18. Varun, Y.; Augustus, H.; Panda, N.; Singh, S.A. Enhanced photocatalytic activity of TiO_2–NiO heterojunctions supported on alumina for malachite green degradation. *Int. J. Environ. Sci. Technol.* **2023**, *20*, 3023–3038. [CrossRef]
19. Chen, L.J.; Lee, C.R.; Chuang, Y.J.; Wu, Z.H.; Chen, C.E.Y. Synthesis and Optical Properties of Lead-Free Cesium Tin Halide Perovskite Quantum Rods with High-Performance Solar Cell Application. *J. Phys. Chem. Lett.* **2016**, *7*, 5028–5035. [CrossRef] [PubMed]
20. Li, X.M.; Wu, Y.; Zhang, S.L.; Cai, B.; Gu, Y.; Song, J.Z.; Zeng, H.B. $CsPbX_3$Quantum Dots for Lighting and Displays: Room-Temperature Synthesis, Photoluminescence Superiorities, Underlying Origins and White Light-Emitting Diodes. *Adv. Funct. Mater.* **2016**, *26*, 2435–2445. [CrossRef]
21. Qian, J.; Sun, F.; Qin, L. Hydrothermal synthesis of zeolitic imidazolate framework-67 (ZIF-67) nanocrystals. *Mater. Lett.* **2012**, *82*, 220–223. [CrossRef]
22. Jiang, J.; Yu, J.; Cao, S. Au/PtO nanoparticle-modified g-C_3N_4 for plasmon-enhanced photocatalytic hydrogen evolution under visible light. *J. Colloid Interface Sci.* **2016**, *461*, 56–63. [CrossRef] [PubMed]
23. Huang, L.; Huang, X.J.; Yan, J.; Liu, Y.H.; Jiang, H.; Zhang, H.G.; Tang, J.F.; Liu, Q. Research progresses on the application of perovskite in adsorption and photocatalytic removal of water pollutants. *J. Hazard. Mater.* **2023**, *442*, 130024. [CrossRef] [PubMed]
24. Gupta, S.; Bendikov, T.; Hodes, G.; Cahen, D. $CsSnBr_3$, A Lead-Free Halide Perovskite for Long-Term Solar Cell Application: Insights on SnF_2 Addition. *ACS Energy Lett.* **2016**, *1*, 1028–1033. [CrossRef]
25. Wang, S.F.; Li, Y.; Liu, Q.; Wang, J.Y.; Zhao, Y.J.; Cai, Y.W.; Li, H.; Chen, Z.S. Photo-/electro-/piezo-catalytic elimination of environmental pollutants. *J. Photochem. Photobiol. A Chem.* **2023**, *437*, 114435. [CrossRef]
26. Popovic, V.; Jovanovic, D.S.; Miletic, Z.; Milovanovic, J.; Lucic, A.; Rakonjac, L.; Miljkovic, D. The evaluation of hazardous element content in the needles of the Norway spruce (*Picea abies* L.) that originated from anthropogenic activities in the vicinity of the native habitats. *Environ. Monit. Assess.* **2022**, *195*, 109. [CrossRef]
27. Moghe, D.; Wang, L.L.; Traverse, C.J.; Redoute, A.; Sponseller, M.; Brown, P.R.; Bulovic, V. All Vapor-Deposited Lead-Free Doped $CsSnBr_3$ Planar Solar Cells. *Nano Energy* **2016**, *28*, 469–474. [CrossRef]
28. Lafta, M.A.; Ammar, S.H. Synthesis and photocatalytic activity of polyoxometalates immobilized onto g-C_3N_4/ZIF-67 heterostructures. *Mater. Sci. Semicond. Process.* **2023**, *153*, 107131. [CrossRef]
29. Zhong, R.Q.; Liao, H.W.; Deng, Q.L.; Zou, X.H.; Wu, L.X. Preparation of a novel composite photocatalyst BiOBr/ZIF-67 for enhanced visible-light photocatalytic degradation of RhB. *J. Mol. Struct.* **2022**, *1259*, 132768. [CrossRef]
30. Tran, N.T.; Trung, L.G.; Nguyen, M.K. The degradation of organic dye contaminants in wastewater and solution from highly visible light responsive ZIF-67 monodisperse photocatalyst. *J. Solid State Chem.* **2021**, *300*, 122287. [CrossRef]
31. Flihh, S.M.; Ammar, S.H. Zeolitic imidazolate framework grafted by cobalt tungstate as an efficient photocatalyst for photocatalytic oxidative desulfurization of dibenzothiophene. *Mater. Sci. Semicond. Process.* **2022**, *149*, 106894. [CrossRef]
32. Abdelhameed, R.M.; Abu-Elghait, M.; El-Shahat, M. Hybrid three MOFs composites (ZIF-67@ZIF-8@MIL-125-NH_2): Enhancement the biological and visible-light photocatalytic activity. *J. Environ. Chem. Eng.* **2020**, *8*, 104107. [CrossRef]
33. Khan, I.; Luo, M.S.; Guo, L.; Khan, S.; Shah, S.A.; Khan, I.; Khan, A.; Wang, C.J.; Ai, B.H.; Zaman, S. Synthesis of phosphate-bridged g-C_3N_4/$LaFeO_3$ nanosheets Z-scheme nanocomposites as efficient visible photocatalysts for CO_2 reduction and malachite green degradation. *Appl. Catal. A Gen.* **2022**, *629*, 118418. [CrossRef]
34. Payra, S.; Reddy, K.L.; Sharma, R.S.; Singh, S.; Roy, S. A trade-off between adsorption and photocatalysis over ZIF-derived composite. *J. Hazard. Mater.* **2020**, *393*, 122491. [CrossRef]
35. Zhang, Y.; Jin, Z. Boosting Photocatalytic Hydrogen Evolution Achieved by NiSx Coupled with g-C_3N_4@ZIF-67 Heterojunction. *J. Phys. Chem. C* **2019**, *123*, 18248–18263. [CrossRef]

36. Aredekani, M.A.; Naimi-Jamal, M.R.; Doaee, S.; Rostamnia, S. Solvent-Free Mechanochemical Preparation of Metal-Organic Framework ZIF-67 Impregnated by Pt Nanoparticles for Water Purification. *Catalysts* **2022**, *13*, 9. [CrossRef]
37. Wang, T.; Guo, C.Y.; Zhang, L.; Zhang, L.G.; Cao, X.L.; Akram, N.; Niu, Y.N.; Wang, J.D. Comparison of modulation strategies for enhancing the photocatalytic water splitting performance of metal-organic frameworks. *J. Phys. Chem. Solids* **2023**, *175*, 111223. [CrossRef]
38. Khan, I.; Yuan, A.H.; Khan, S.; Khan, S.; Shah, S.A.; Luo, M.S.; Yaseen, W.; Shen, X.P.; Yaseen, M. Graphitic Carbon Nitride Composites with Gold and ZIF-67 Nanoparticles as Visible-Light-Promoted Catalysts for CO_2 Conversion and Bisphenol A Degradation. *ACS Appl. Nano Mater.* **2022**, *5*, 13404–13416. [CrossRef]
39. Zhang, Z.J.; Wang, W.Z.; Gao, E.P.; Sun, S.M.; Zhang, L. Photocatalysis Coupled with Thermal Effect Induced by SPR on Ag-Loaded Bi_2WO_6 with Enhanced Photocatalytic Activity. *J. Phys. Chem. C* **2012**, *116*, 25898–25903. [CrossRef]
40. Xu, J.; Chang, Y.G.; Zhang, Y.Y.; Ma, S.Y.; Qu, Y.; Xu, C.T. Effect of silver ions on the structure of ZnO and photocatalytic performance of Ag/ZnO composites. *Appl. Surf. Sci.* **2008**, *255*, 1996–1999. [CrossRef]
41. Zhao, Z.W.; Zhang, W.D.; Sun, Y.J.; Yu, J.Y.; Zhang, Y.X.; Wang, H.; Dong, F.; Wu, Z.B. Bi Cocatalyst/Bi_2MoO_6 Microspheres Nanohybrid with SPR-Promoted Visible-Light Photocatalysis. *J. Phys. Chem. C* **2016**, *120*, 11889–11898. [CrossRef]
42. Mei, F.F.; Dai, K.; Zhang, J.F.; Li, W.Y.; Liang, C.H. Construction of Ag SPR-promoted step-scheme porous g-C_3N_4/Ag_3VO_4 heterojunction for improving photocatalytic activity. *Appl. Surf. Sci.* **2019**, *488*, 151–160. [CrossRef]
43. Rayalu, S.S.; Jose, D.; Joshi, M.V.; Mangrulkar, P.A.; Shrestha, K.; Klabunde, K. Photocatalytic water splitting on Au/TiO_2 nanocomposites synthesized through various routes: Enhancement in photocatalytic activity due to SPR effect. *Appl. Catal. B Environ.* **2013**, *142–143*, 684–693. [CrossRef]
44. Homola, J.; Piliarik, M. Surface Plasmon Resonance (SPR) Sensors. In *Surface Plasmon Resonance Based Sensors*; Springer: Berlin/Heidelberg, Germany, 2006; pp. 45–67.
45. Lin, F.; Shao, B.; Li, Z.; Zhang, J.Y.; Wang, H.; Zhang, S.H.; Haruta, M.; Huang, J.H. Visible light photocatalysis over solid acid: Enhanced by gold plasmonic effect. *Appl. Catal. B Environ.* **2017**, *218*, 480–487. [CrossRef]
46. Gong, Z.; Ji, J.L.; Wang, J.G. Photocatalytic Reversible Reactions Driven by Localized Surface Plasmon Resonance. *Catalysts* **2019**, *9*, 193. [CrossRef]
47. Liu, W.; Shen, J.; Chen, H.Q.; Liu, Q.Q.; Yang, X.F.; Tang, H.; Peng, Z. Localized Surface Plasmon Resonance Induced Band Gap Regulation Governing the Excellent Photocatalytic Performance of Ag/g-C_3N_4 Heterostructure. *J. Nanosci. Nanotechnol.* **2019**, *19*, 5582–5590. [CrossRef]
48. Chen, K.; Wang, H. Plasmon-driven photocatalytic molecular transformations on metallic nanostructure surfaces: Mechanistic insights gained from plasmon-enhanced Raman spectroscopy. *Mol. Syst. Des. Eng.* **2021**, *6*, 250–280. [CrossRef]
49. Zhidkov, I.S.; Kurmaev, E.Z.; Cholakh, S.O.; Fazio, E.; D'Urso, L. XPS study of interactions between linear carbon chains and colloidal Au nanoparticles. *Mendeleev Commun.* **2020**, *30*, 285–287. [CrossRef]
50. Luo, Q.; Zhang, C.X.; Deng, X.S.; Zhu, H.B.; Li, Z.Q.; Wang, Z.B.; Chen, X.H.; Huang, S.M. Plasmonic Effects of Metallic Nanoparticles on Enhancing Performance of Perovskite Solar Cells. *ACS Appl. Mater. Interfaces* **2017**, *9*, 34821–34832. [CrossRef]
51. Hartmann, C.; Gupta, S.; Bendikov, T.; Kozina, X.; Kunze, T.; Felix, R.; Hodes, G.; Wilks, R.; Cahen, D.; Bar, M. Impact of SnF_2 Addition on the Chemical and Electronic Surface Structure of $CsSnBr_3$. *ACS Appl. Mater. Interfaces* **2020**, *12*, 12353–12361. [CrossRef]
52. Chen, S.; Pan, B.; Zeng, L.Q.; Luo, S.J.; Wang, X.X.; Su, W.Y. $La_2Sn_2O_7$ enhanced photocatalytic CO_2 reduction with H_2O by deposition of Au co-catalyst. *RSC Adv.* **2017**, *7*, 14186–14191. [CrossRef]
53. Reyes-Pérez, F.; Gallardo, J.J.; Aguilar, T.; Alcantara, R.; Fernandez-Lorenzo, C.; Navas, J. Visible-Light-Enhanced Photocatalytic Activity of Totally Inorganic Halide-Based Perovskite. *ChemistrySelect* **2018**, *3*, 10226–10235. [CrossRef]
54. Yamashita, H.; Miura, Y.; Mori, K.; Ohmichi, T.; Sakata, M.; Mori, H. Synthesize of nano-sized Pd metal catalyst on Ti-containing zeolite using a photo-assisted deposition (PAD) method. *Catal. Lett.* **2007**, *114*, 75–78. [CrossRef]
55. Luo, J.Q.; Zhang, W.W.; Yang, H.B.; Fan, Q.W.; Xiong, F.Q.; Liu, S.J.; Li, D.S.; Liu, B. Halide perovskite composites for photocatalysis: A mini review. *EcoMat* **2021**, *3*, e12079. [CrossRef]
56. Cai, M.; Loague, Q.; Morris, A.J. Design Rules for Efficient Charge Transfer in Metal-Organic Framework Films: The Pore Size Effect. *J. Phys. Chem. Lett.* **2020**, *11*, 702–709. [CrossRef]